



The Flow of Triboplasma

Keiji Nakayama¹ · Fumio Yagasaki²

Received: 25 February 2019 / Accepted: 15 May 2019 / Published online: 25 May 2019
© Springer Science+Business Media, LLC, part of Springer Nature 2019

Abstract

Previously triboplasma was discovered in the rear gap of the sliding contact. Recently, the temperature of the triboplasma was successfully measured and demonstrated that the triboplasma is the non-equilibrium low-temperature plasma. During the course of the temperature rise distribution measurement of the triboplasma, flow of the triboplasma was observed. In this article, the triboplasma flow behaviors were investigated by measuring the triboplasma temperature rise distribution using a highly sensitive microscopic infrared camera. The measurement was performed in the tribosystem while a diamond pin with a tip radius of 4 mm slides on a sapphire disk with the wear track diameter of 40 mm in dry sliding in the ambient air under the normal forces of $F_N = 1$ N and 2 N and the disk rotational velocities of $\omega = 10, 20, 50, 100,$ and 155 rpm, which correspond to the sliding velocities of $V = 0.021, 0.042, 0.105, 0.21,$ and 0.324 m/s, respectively. In the experiments, the pin and disk specimens were warmed to raise the negligibly small temperature rise of the rear plasma tail region to the infrared camera imaging detection level by transferring the specimen's heat to the plasma. Two types of plasma flows have been observed. One of them is a lamellar flow under the rotational velocity region of $\omega \leq 10$ rpm ($V \leq 0.021$ m/s). This laminar flow transits to the turbulent one under $\omega \geq 20$ rpm ($V \geq 0.042$ m/s). At the lamellar flow region, the triboplasma flows in the direction of sliding. However, at the turbulent flow region, the plasma flow direction shifts clockwise from the sliding line to the direction of disk rotation. The flow angle between the sliding line and the plasma flow one increases with the rotational velocity due to the centrifugal forces by disk rotation.

Keywords Plasma · Triboplasma · Temperature distribution · Low-temperature plasma · Plasma flow · Tribocharging

1 Introduction

Triboplasma was discovered in the rear gap of the sliding contact in 2001 [1]. The triboplasma is the plasma generated by the relative motion of the mating two surfaces, i.e., by rubbing. The rubbing causes first tribocharging, which generates intense electric field in the gap of sliding contact. Then the electric field accelerates the electrons which are emitted from the negatively charged surface of the two mating rubbing surfaces. The accelerated electrons interact with the air molecules producing additional electrons leading to the electron avalanche process in the gap of the sliding contact to generate plasma, i.e., the triboplasma. The

mechanism of the triboplasma generation has been described in detail using the most recent model of the triboelectromagnetic phenomena, which embrace triboplasma generation, triboemission of electrons, negative and positive ions, radicals and photons, tribocharging and post emission of electrons and photons, in the previous article [2].

Based on the temperature level, plasma is classified into two groups, i.e., the high-temperature plasma [3, 4] and the non-equilibrium low-temperature plasma [5–7]. Very recently, temperature of the triboplasma was successfully measured in the tribosystem of a diamond pin sliding on a rotating disk. The experiment showed that the maximum temperature rise of the plasma was so small of 0.69 °C, which demonstrated that the triboplasma is the non-equilibrium low-temperature plasma [8]. This is because the maximum temperature of the plasma gas including ions, radical and neutral molecules are so small of 0.69 °C, but the energy, i.e. the temperatures, of the electrons should be so great as reported previously [9]. The measured temperature distribution showed also that the triboplasma temperature

✉ Keiji Nakayama
keiji.nakayama.iom@gmail.com

¹ Institute of Mesotechnology, 2-2-1-201 Nakahara,
Kashiwa 277-0085, Japan

² Ken Automation Inc., Hiranuma 1-11-12, Nishi-ku,
Yokohama 220-0023, Japan

rise depends on the tribocharge distribution on the frictional track, since the tribocharge-induced electric fields accelerate the electrons which generate the plasma gas. [2].

As the smaller specimen moves on the mating surface, triboplasma gas originated at the sliding contact should flow through the rear contact gap toward the exit. This plasma gas flow gives the tailing to the triboplasma. However, no work on the triboplasma flow behavior has been reported so far.

In the present article, the flow behaviors of the triboplasma were investigated by measuring the triboplasma temperature rise distribution, since the previous report showed that the triboplasma temperature rise distribution clearly showed the image of the triboplasma distribution. The triboplasma temperature rise was only $0.69\text{ }^{\circ}\text{C}$ as described above even at the center of the triboplasma inside of the rear gap, whereas the temperature rise at the plasma tailing region was too weak to be detected for imaging by the infrared camera. Then, in the present experiments, the pin and disk specimens were warmed to increase the negligibly small temperature rise of the rear plasma tail region to the infrared camera detection level by transferring the specimen's heat to the plasma. Then we succeeded to measure the triboplasma flow image. Two types of flow were observed, i.e., the lamellar and the turbulent flows [9, 10]. Further, the plasma flow direction was found to shift to the direction of the disk rotation by the centrifugal forces.

2 Experimental Procedure

Triboplasma flow characteristics were investigated by measuring the temperature rise distribution images using the pin and disk specimens warmed by hot air stream before the sliding experiments. These warmed specimens are called *the warmed specimens* from now on. For comparison, the temperature rise distributions were also measured for the specimens having the room temperature without warming. These specimens are also called *the non-warmed specimens*.

Figure 1 shows a schematic representation of the apparatus to measure the triboplasma temperature rise distribution above the ambient one, ΔT , using the microscopic high accuracy infrared camera (IRC) (FLIRATS Co. Ltd. SC7600-BB). The sensitive wavelength of the camera was from $2.5\text{ }\mu\text{m}$ to $5.0\text{ }\mu\text{m}$. The temperature rise of the triboplasma generated in the gap of the sliding contact and the vicinity were measured while sliding a diamond pin with a tip radius of $R=4\text{ mm}$ on a sapphire disk (single crystal Al_2O_3) with a diameter of 50 mm and the thickness of 1 mm under dry sliding in a room temperature of $T_R=26\text{ }^{\circ}\text{C}$, in the ambient room air with the relative humidity of $H_R=20\%$. The diamond pin was embedded into the cylindrical Ti bar having a diameter of 2 mm and an included angle of 120° to avoid the magnetization of the pin observed such

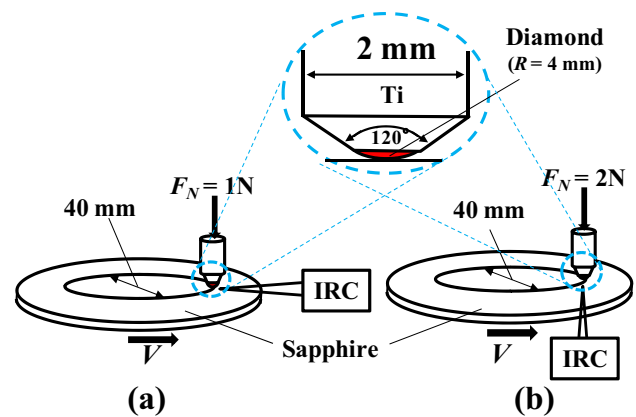


Fig. 1 Pin-on-disk tribometer installed with an infrared camera, IRC: **a** side image measurement, **b** plane image measurement

as Fe. The side image of the temperature rise distribution was measured from the horizontal direction with an angle of several degrees from the sapphire disk surface as seen in Fig. 1a, whereas the plane image was measured vertically through the sapphire disk as seen in Fig. 1b. The resolution of the IR camera was $15\text{ }\mu\text{m}/\text{pixel}$ and the integration time (exposure time) was 2.35 ms . The friction experiments were performed under the normal force $F_N=1\text{ N}$ for the side image and $F_N=2\text{ N}$ for the plane image, respectively, and the rotational velocities of $\omega=10, 20, 50, 100,$ and 155 rpm , which correspond to the sliding velocities of $V=0.021, 0.042, 0.105, 0.21, 0.324\text{ m/s}$, respectively, under the wear track diameter of 40 mm . The maximum Hertzian contact pressures under $F_N=1$ and 2 N were $P_{\text{max},1\text{N}}=952\text{ MPa}$ and $P_{\text{max},2\text{N}}=1200\text{ MPa}$, respectively, whereas the mean Hertzian contact pressures under $F_N=1$ and 2 N were $P_{\text{mean},1\text{N}}=634\text{ MPa}$ and $P_{\text{mean},2\text{N}}=800\text{ MPa}$, respectively. They were calculated using the material parameters of diamond and sapphire. Young's modulus of diamond and sapphire is $E_{\text{dia}}=1050\text{ GPa}$ and $E_{\text{sap}}=335\text{ GPa}$, respectively, whereas Poisson ratio of diamond and sapphire is $\nu_{\text{dia}}=0.1$ and $\nu_{\text{sap}}=0.25$, respectively. The test specimens were cleaned with the solvents of *n*-hexane, ethanol, and then acetone in an ultrasonic bath. The adsorbed solvents molecules were then removed from the pin and disk specimen surfaces by hot air stream.

3 Results and Discussion

3.1 Laminar Flow Under $\omega \leq 10\text{ rpm}$ ($V=0.021\text{ m/s}$)

3.1.1 Side and Plane Images of the Lamellar Flow

Figure 2a, b shows the typical side and plane images of the temperature rise distribution, ΔT , measured by the IR

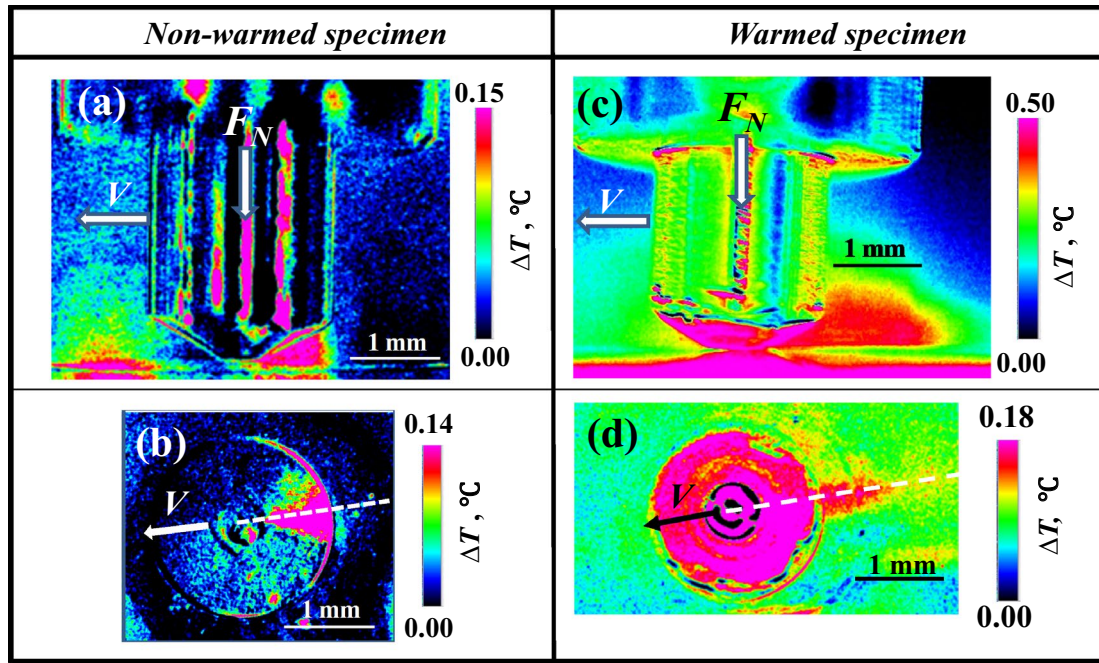


Fig. 2 Typical side and plane images of the temperature rise, ΔT , distributions above the room temperature in the *non-warmed* specimens (a, b) and those in the *warmed* specimens (c, d), respectively, under $\omega = 10$ rpm ($V = 0.021$ m/s)

camera from the side-ward and the vertical-ward through the sapphire disk in the tribosystem of the *non-warmed* diamond pin sliding against the *non-warmed* sapphire disk at the sliding time of $t = 0.1$ s under $\omega = 10$ rpm ($V = 0.021$ m/s) and $F_N = 1$ N and $F_N = 2$ N, respectively. However, Fig. 2c, d shows those images measured, under the same sliding conditions, for the *warmed* specimens at $t = 1.0$ s. In Fig. 2a in the *non-warmed* specimens, no plasma flow image is seen in the rear outside region of the contact gap, though Fig. 2b suggests the existence of weak plasma flow. On the other hand, in Fig. 2c, d in the *warmed* specimens, the tribo-plasma is clearly flowing out of the rear gap along the wear track. Front plasma is sometimes generated in the front outside of the sliding contact as seen in Fig. 2a, but not in Fig. 2c and d. This is because the front plasma is generated only when enough charges remain even after consuming the main charges for generating the rear plasma [7].

Figure 3 shows the tribo-plasma temperature rise distribution in the *non-warmed* specimens under $\omega = 10$ rpm ($V = 0.021$ m/s) and the temperature rise profile along the a-b-c line. The temperature rise image in the *non-warmed* specimens shows no plasma flowing out as described above, but the temperature rise profile shows clearly that the plasma is flowing out of the rear gap for the distance of $\Delta l = 0.8$ mm. The plasma temperature rise of $\Delta T = 0.15$ °C inside the gap decreases first steeply and then gradually to the ambient room temperature of $\Delta T = 0.00$ °C. This means

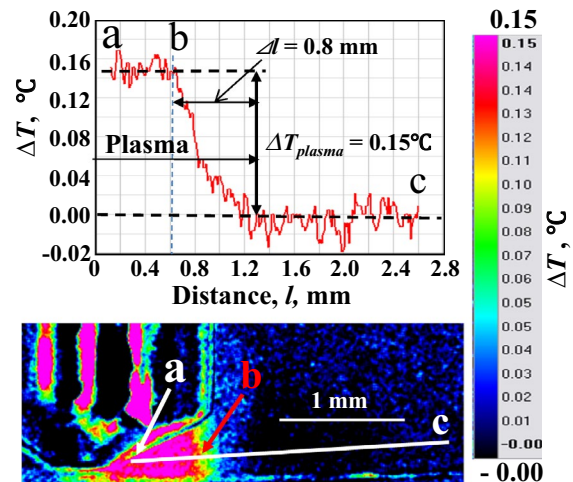


Fig. 3 Side image of the temperature rise, ΔT , distribution and the temperature rise profile along the a-b-c line in the *non-warmed* specimens at $t = 0.1$ s under $\omega = 10$ rpm ($V = 0.021$ m/s) and $F_N = 1$ N

that the imaging level of the IR camera is not enough to give the plasma image in the tailing region under $\Delta T < 0.15$ °C.

To get the plasma tailing image, i.e., the plasma flowing image, we tried to raise the small temperature rise of $\Delta T < 0.15$ °C to the image detection level of the IR camera by warming the pin and disk specimens to transfer their heat to the plasma. Figure 4 shows the side image of the temperature rise distribution in the *warmed* specimens

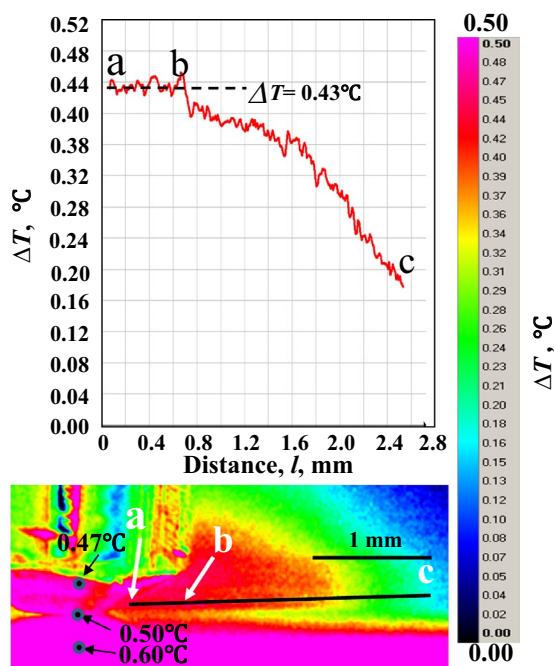


Fig. 4 Side image of the temperature rise, ΔT , distribution and the temperature rise profile along the a-b-c line in the warmed specimens at $t = 1.0$ s under $\omega = 10$ rpm ($V = 0.021$ m/s) and $F_N = 1$ N

under $\omega = 10$ rpm ($V = 0.021$ m/s) and the temperature rise profile along the a-b-c line. The temperatures of the pin, the sliding contact, and the disk were raised from the ambient temperature of $\Delta T = 0.00$ °C to $\Delta T_{pin} = 0.47$ °C, $\Delta T_{contact} = 0.50$ °C, and $\Delta T_{disk} = 0.60$ °C, respectively. The heat of the warmed specimens transferred to the plasma inside the specimen gap and raised the plasma temperature from the $\Delta T_{plasma} = 0.15$ °C of the non-warmed specimens to the $\Delta T_{plasma} = 0.43$ °C of the warmed specimen by 0.28 °C. The warmed plasma temperature rise decreases first gradually and then rather steeply with the distance from the end of the specimen gap. The temperature rise profile shows smooth temperature decrease and the plasma flow image also has smooth surface. These features demonstrate that the plasma flow under $\omega = 10$ rpm ($V = 0.021$ m/s) is the lamellar one.

The plasma flow size in the warmed specimens is much greater than that in the non-warmed specimens. This is probably due to that the plasma measured in the warmed specimens by the temperature rise measurement contains non-plasma gas where the electrons, ions, and radicals have already ceased because of their short life. However, it is difficult to distinguish the plasma region and non-plasma region in the temperature measurement technique. Then, in this report, we call the whole plasma flow region detected in the warmed specimens the plasma flow region.

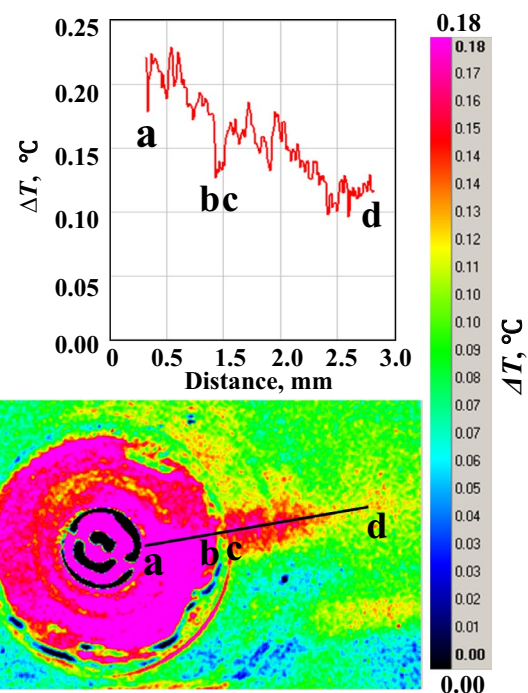


Fig. 5 Plane image of the temperature rise, ΔT , distribution and the temperature rise profile along the a-b-c-d line in the warmed specimens at $t = 4.5$ s under $\omega = 10$ rpm ($V = 0.021$ m/s) and $F_N = 2$ N

Figure 5 shows the plane image of the temperature rise and the temperature rise profile along the a-b-c-d line in the warmed specimens under $\omega = 10$ rpm ($V = 0.021$ m/s). The temperature rise in the a-b region shows the combined temperature rise of the plasma and the warmed pin surface, whereas the temperature rise in the c-d region shows plasma temperature rise itself, which decreases gradually with the distance to the rear direction of the sliding. The plasma image shows that the plasma is flowing out along the wear track. The linear flow shows also that it is a lamellar flow.

It is clear that the temperature rise distribution image of the plasma measured for the warmed specimens under $\omega = 10$ rpm ($V = 0.021$ m/s) give the plasma flow image. Namely, we can investigate the plasma flow behaviors using the warmed specimens. Then the plasma flow behaviors are investigated using the warmed pin and the disk specimens for other rotational velocities.

3.1.2 Time Dependence Nature of the Lamellar Flow

Figure 6 shows the time dependence of the side images of the plasma temperature rise distribution in the warmed test specimens under $\omega = 10$ rpm ($V = 0.021$ m/s) and $F_N = 1$ N at $t = 0.01$ to 5.0 s, where the time of one disk revolution, t_{1rev} , is 6.0 s. It can be seen from Fig. 6 that the plasma size and intensity are steeply growing from $t = 0.01$ s, reaching a maximum at $t = 1.50$ s and then decreases with time,

Fig. 6 Time dependence of the side image of the temperature rise, ΔT , distributions for the warmed specimens under $\omega = 10$ rpm ($V = 0.021$ m/s) where the time of one revolution, t_{1rev} is 6.0 s

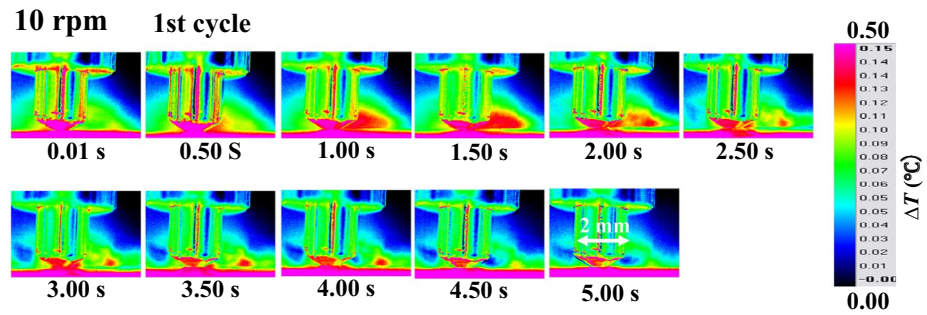
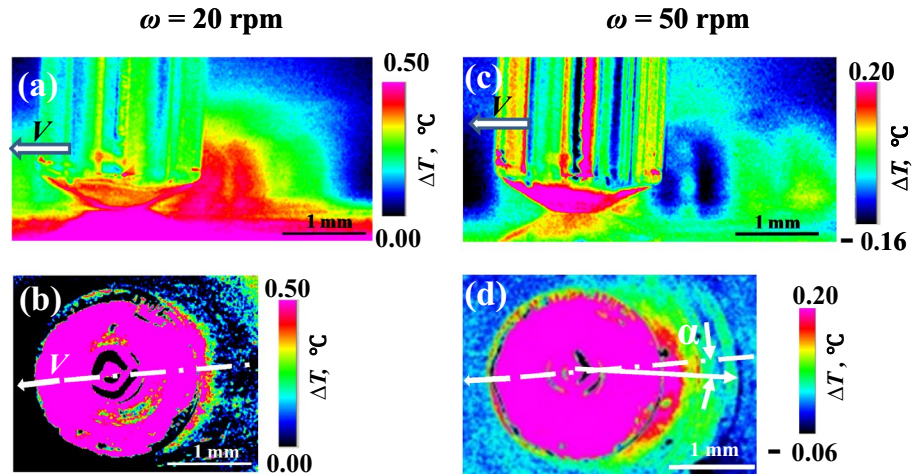


Fig. 7 Typical side (a) and plane (b) images of the temperature rise, ΔT , distributions in the warmed specimens under $\omega = 20$ rpm ($V = 0.042$ m/s) and those (c, d) under $\omega = 50$ rpm ($V = 0.105$ m/s)



i.e., with the sliding distance. After reaching the maximum in size and intensity at $t = 1.5$ s, the plasma density also decreases. This time dependence nature of the temperature rise distribution, i.e., plasma distribution, is caused by sliding of the pin on the tribocharge distributed wear track surface as reported previously [2].

3.2 Turbulent Flow Under $\omega \geq 20$ rpm ($V = 0.042$ m/s)

3.2.1 Side and Plane Images of the Turbulent Flow

Figure 7a, b shows the typical side and plane images of the temperature rise distributions in the warmed specimens under $\omega = 20$ rpm ($V = 0.042$ m/s), whereas Fig. 7c, d shows those under $\omega = 50$ rpm ($V = 0.105$ m/s), respectively. It is clearly seen in Fig. 7a, c that the plasma is flowing out of the contact gap not in the lamellar flow, but in the turbulent one which flows out in a swirl. The plane images in Fig. 7b, d show also that the plasma flow is the turbulent one spreading rectangular to the sliding direction. The center of the plasma flow under $\omega = 20$ rpm ($V = 0.042$ m/s) seems to be almost on the wear track. However, the center of the flow under $\omega = 50$ rpm ($V = 0.105$ m/s) is not on the wear track, but it shifts clockwise by an angle of about $\alpha = 5^\circ$ to the disk rotation direction. This shift must be caused by the centrifugal forces caused by the rotation of the disk specimen.

Figure 8a, b shows the side images of the temperature rise distributions and the temperature rise profiles along the a-b-c-d-e-f-g lines under $\omega = 20$ rpm ($V = 0.042$ m/s) (a) and $\omega = 50$ rpm ($V = 0.105$ m/s) (b), respectively. The images and the profiles in Fig. 8a, b show clearly the characteristics of the turbulent flow of the plasma which is whirling. The temperature rise at “c” and “e” under $\omega = 50$ rpm ($V = 0.105$ m/s) has the negative values of $\Delta T = -0.13$ °C and -0.16 °C, respectively. Namely, the temperatures of these regions are lower than the ambient one. These negative temperature rises must be caused by the local adiabatic air expansion caused by the turbulent flow.

Figure 9a, b shows the side images of the temperature rise distributions and the temperature rise profiles along the a-b-c-d-e lines under $\omega = 100$ rpm ($V = 0.21$ m/s) and $\omega = 155$ rpm ($V = 0.324$ m/s), respectively, showing that the plasma flow is also the turbulent flow in both $\omega = 100$ rpm ($V = 0.21$ m/s) and 155 rpm ($V = 0.324$ m/s). In 100 rpm ($V = 0.21$ m/s), the plasma is stretched to the rear direction, whereas the plasma under $\omega = 155$ rpm ($V = 0.324$ m/s) is shorter than that in $\omega = 100$ rpm ($V = 0.21$ m/s) suggesting that the plasma tail is torn off by the higher disk rotation (higher sliding velocity).

Figure 10a, b shows the plane images of the temperature rise distributions and the temperature rise profiles along the a-b-c-d lines under $\omega = 20$ rpm ($V = 0.042$ m/s) and

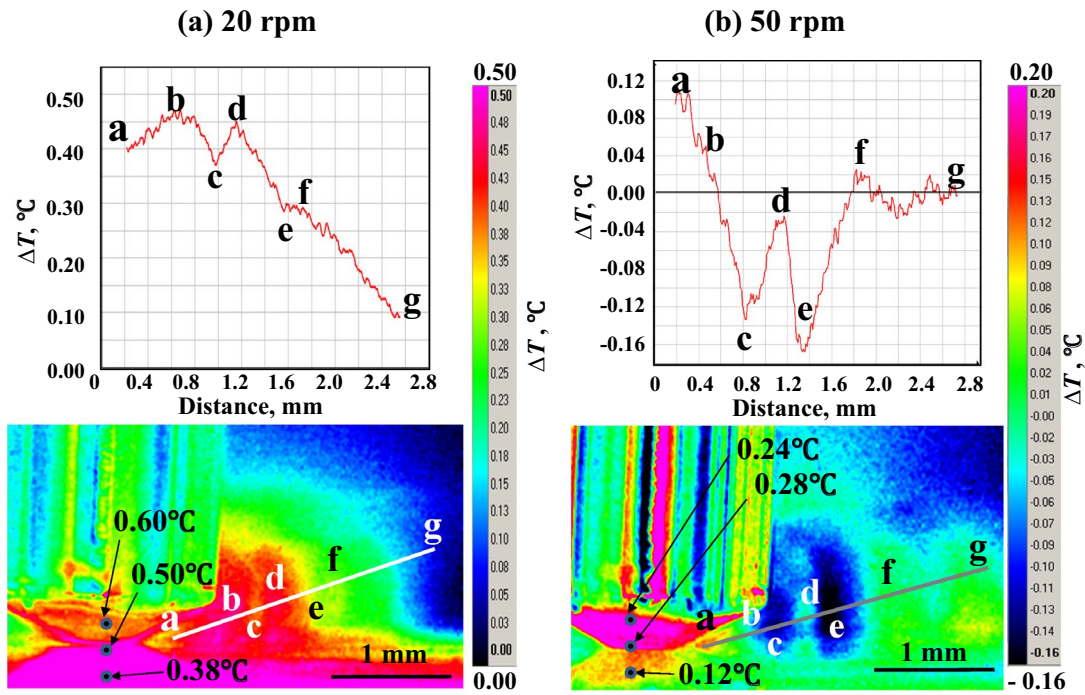


Fig. 8 Side image of the temperature rise, ΔT , distribution and the temperature rise profile along the a-b-c-d-e line in the *warmed* specimens at $t = 1.50$ s under $\omega = 20$ rpm ($V = 0.042$ m/s) (a) and those at $t = 0.09$ s under $\omega = 50$ rpm ($V = 0.105$ m/s) (b), respectively

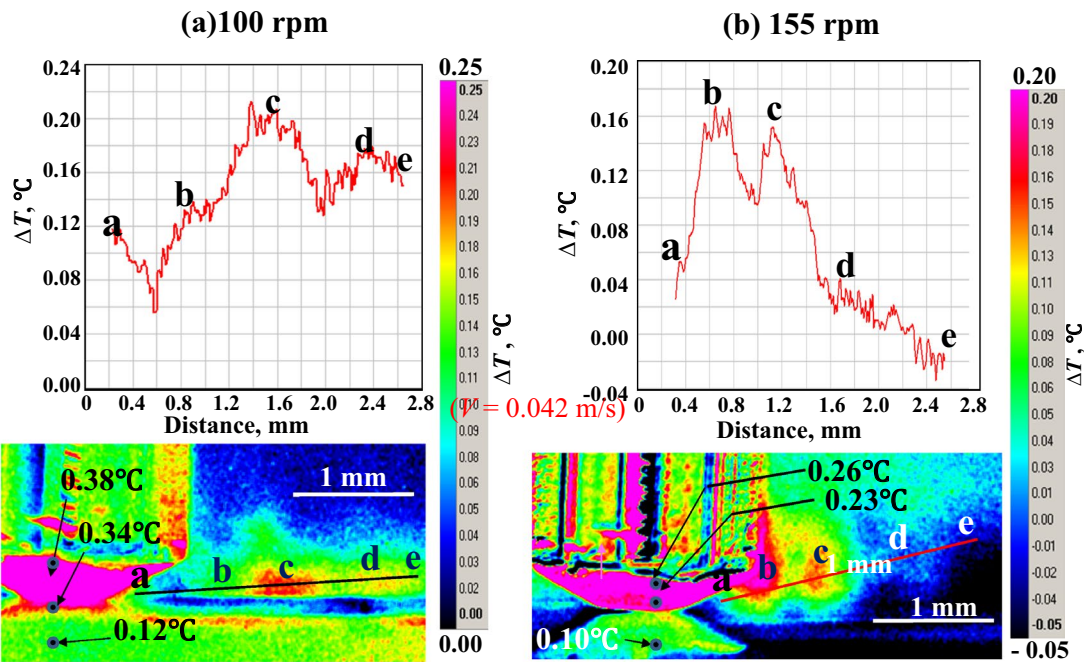


Fig. 9 Side image of the temperature rise, ΔT , distribution and the temperature rise profile along the a-b-c-d-e line in the *warmed* specimens at $t = 0.1$ s under $\omega = 100$ rpm ($V = 0.21$ m/s) (a) and those at $t = 0.05$ s under $\omega = 155$ rpm ($V = 0.324$ m/s) (b)

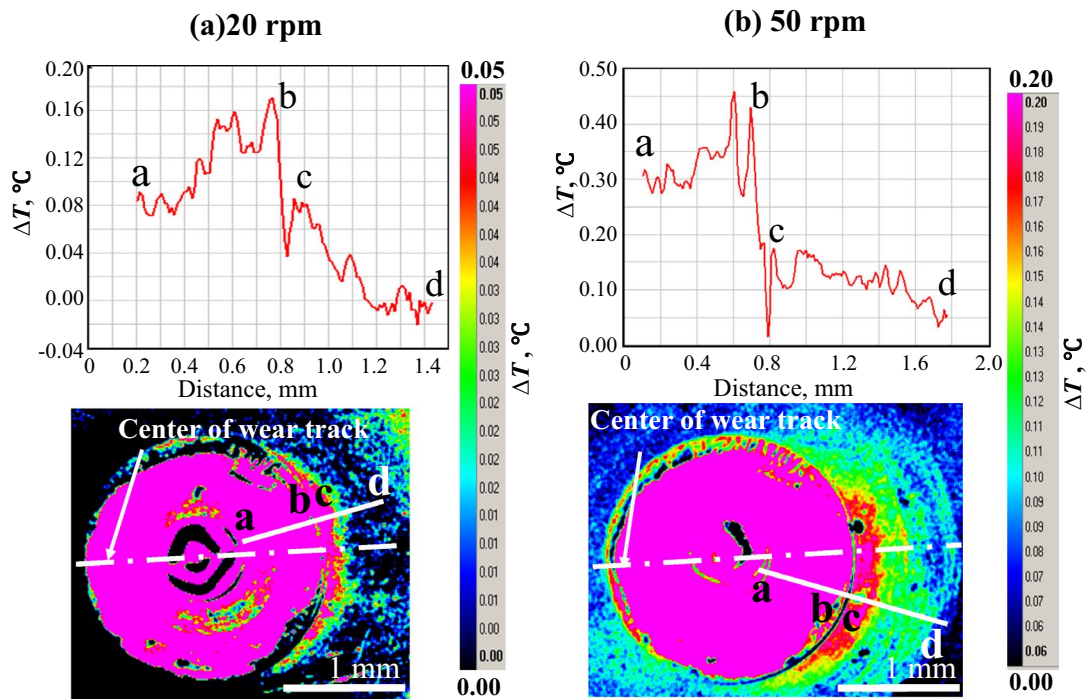


Fig. 10 Plane image of the temperature rise distribution and the temperature rise profile along the a-b-c-d line in the warmed specimens at $t=0.01$ s under $\omega=20$ rpm ($V=0.042$ m/s) (a) and those at $t=0.20$ s under $\omega=50$ rpm ($V=0.105$ m/s) (b)

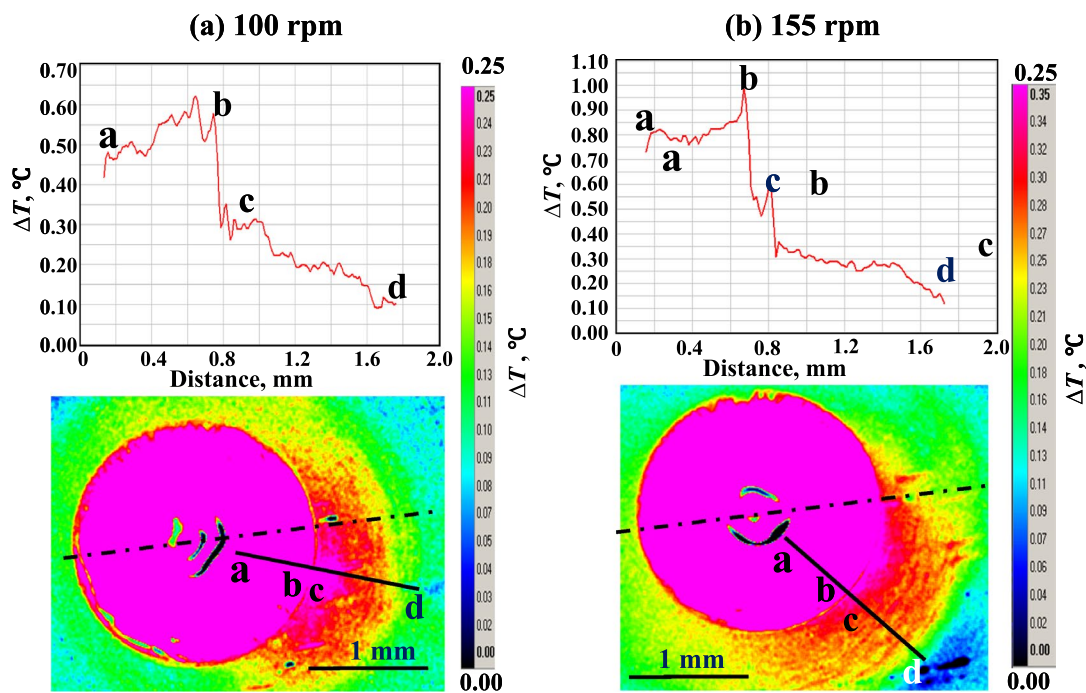


Fig. 11 Plane image of the temperature rise, ΔT , distribution and the temperature rise profile along the a-b-c line in the warmed specimens at $t=0.01$ s under $\omega=100$ rpm ($V=0.21$ m/s) (a) and those at $t=0.05$ s under $\omega=155$ rpm ($V=0.324$ m/s) (b)

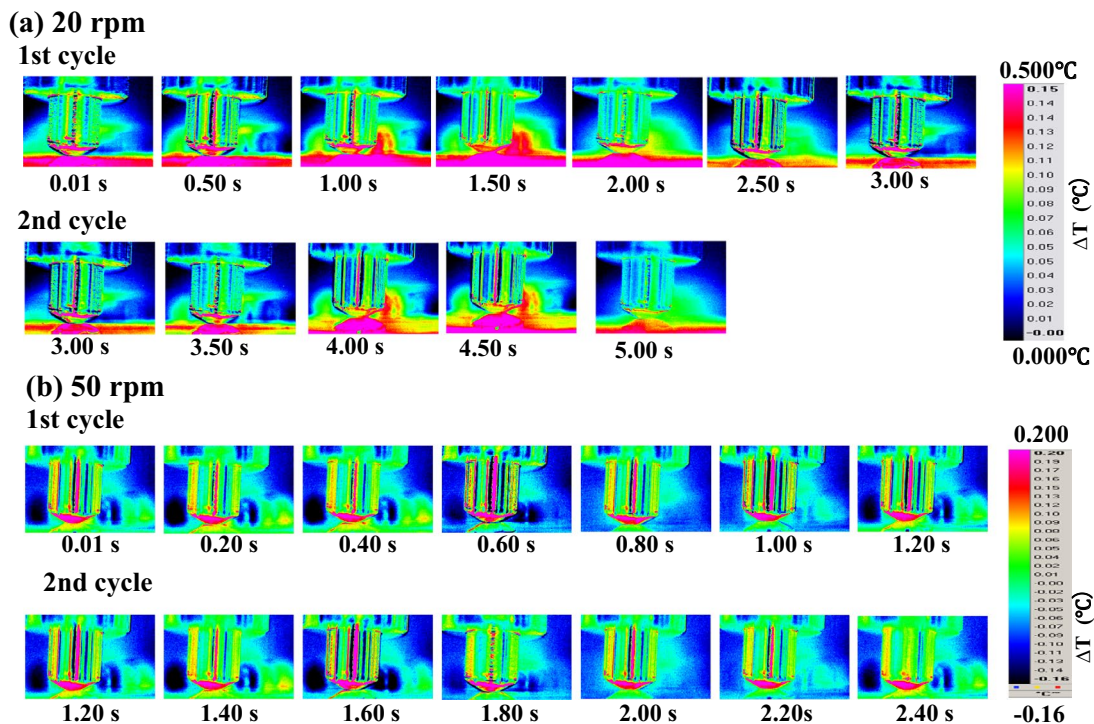


Fig. 12 Time dependence of the side images of the temperature rise, ΔT , distributions for the warmed specimens under $\omega=20$ rpm ($V=0.042$ m/s) with $t_{Irev}=3.0$ s (a) and those under $\omega=50$ rpm ($V=0.105$ m/s) with $t_{Irev}=1.2$ s (b)

50 rpm ($V=0.105$ m/s), respectively, whereas Fig. 11a, b shows those under $\omega=100$ rpm ($V=0.21$ m/s) and 155 rpm ($V=0.324$ m/s), respectively. In all those figures, the temperature rises in the a-b regions show the combined temperature rises of the warmed tribo-plasma and the warmed pin specimens, whereas that in c-d region shows the warmed plasma temperature rise, as described above. The combined temperature rise profiles in the a-b gap regions are not smooth but rough suggesting that the plasma flow is not the lamellar but the turbulent one even inside the gap. Whereas the warmed plasma temperature rise profiles in the c-d regions are also rough showing the turbulent flows to the rear outward. Comparison of these plane images shows that the angle between the sliding direction and the plasma flow direction increases clockwise to the direction of the disk rotation with the rotational velocities.

3.2.2 Time Dependence Nature of the Turbulent Flow

Figure 12a, b shows the time dependence natures of the side images of the plasma temperature rise distribution in the warmed specimens under $\omega=20$ rpm ($V=0.042$ m/s) with $t_{Irev}=3.0$ s and those under $\omega=50$ rpm ($V=0.105$ m/s) with $t_{Irev}=1.20$ s, respectively. It is clearly seen in both time dependence natures of 20 ($V=0.042$ m/s) and 50 rpm ($V=0.105$ m/s) that the plasma flows are the turbulent one

as described above. In 20 rpm ($V=0.042$ m/s), the size and intensity of the plasma flow increases from $t=0.01$ s, reaching the maximum at $t=1.50$ s and then decreases to the minimum at the end of the first cycle of $t=3.00$ s, at which the second cycle of the rotation starts. The time dependence of the plasma flow behavior in the first cycle is repeated in the second cycle, though the side image at the end of the second cycle at $t=6.00$ s is not given. This is because the tribocharge distribution on the wear track surface does almost not change with the repeated sliding, i.e., it is almost independent of the repeated sliding. Therefore, the time dependence nature of the tribo-plasma generation is almost independent of the repeated sliding cycle. This independence of the time dependence nature of the plasma generation is also clearly observed under 50 rpm ($V=0.105$ m/s) in Fig. 12b.

Figure 13a, b shows the time dependence natures of the tribo-plasma flow behaviors measured by the side images of the temperature rise distribution in the warmed specimens under $\omega=100$ rpm ($V=0.21$ m/s) and 155 rpm ($V=0.324$ m/s), respectively. It is also seen in these figures that the time dependence, i.e., sliding distance dependence of the tribo-plasma flow behaviors in the first cycle is correctly repeated in the second cycle. In the higher rotational velocity of 155 rpm ($V=0.324$ m/s), the front plasma is generated showing that the tribocharge is not completely

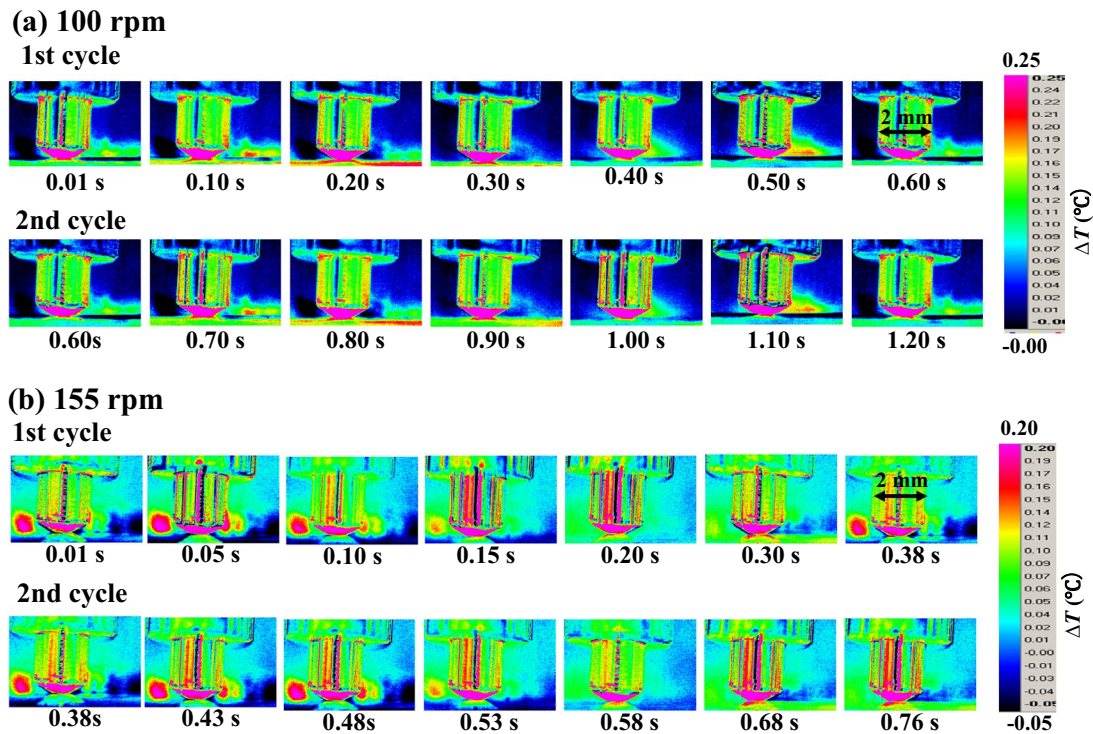


Fig. 13 Time dependence of the side images of the temperature rise, ΔT , distributions for the warmed specimens under $\omega=100$ rpm ($V=0.21$ m/s) with $t_{rev}=0.6$ s (a) and those under $\omega=155$ rpm ($V=0.324$ m/s) with $t_{rev}=0.38$ s (b)

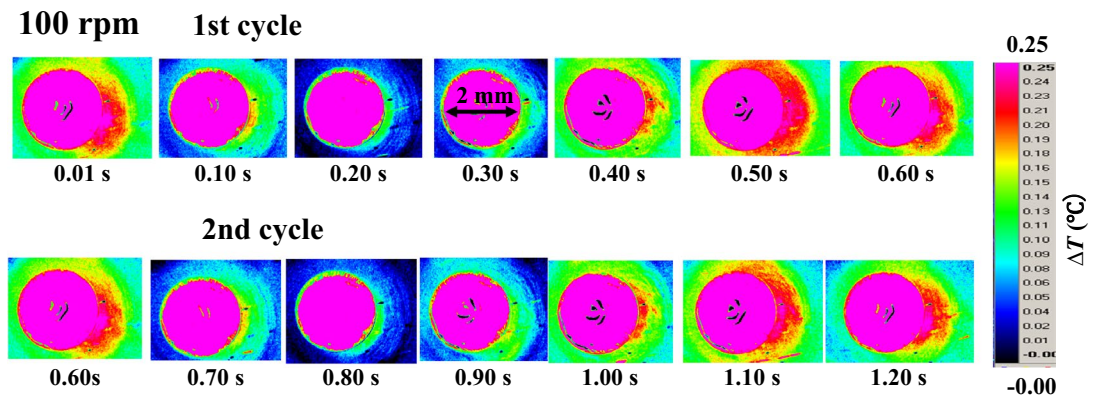


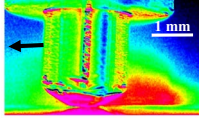
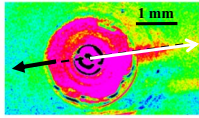
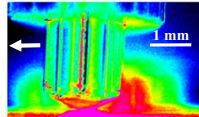
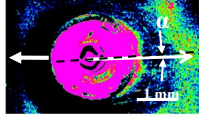
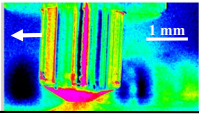
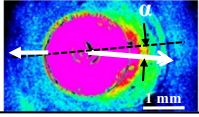
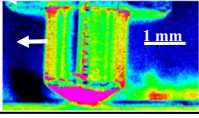
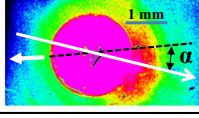
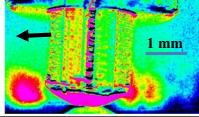
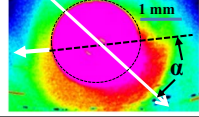
Fig. 14 Time dependence of the plane image of the temperature rise, ΔT , distribution for the warmed specimens under $\omega=100$ rpm ($V=0.21$ m/s) with $t_{rev}=0.6$ s

consumed by the rear triboplasma generation and some charges remained to generate the front plasma [7].

Figure 14 shows the time dependence characteristics of the plane images of the temperature rise distribution in the warmed specimens under $\omega=100$ rpm ($V=0.21$ m/s) with $t_{rev}=0.6$ s. The plasma is flowing out of the gap of the disk and pin, where the plasma flow is first great at

$t=0.01$ s, decreases to the minimum at $t=0.30$ s, and then increases to the end of the first cycle, at which the second cycle starts. The time dependence characteristics are also correctly repeated in the second cycle. The kinds of time dependence nature of the plane image of the triboplasma generation were observed in other rotational velocities of 10, 20, 50, and 155 rpm.

Table 1 Side and plane images, the angle between the wear track and the plasma flow direction, α , and the time of one revolution, t_{Irev} , under various rotational and sliding velocities, ω , V

ω (V)	Side image	Plane image	α	t_{Irev}
10 rpm (0.021 m/s)	$t = 1.00$ s 	$T_{Irev} = 4.5$ s 	0.2°	6.0 s
20 rpm (0.042 m/s)	$t = 1.50$ s 	$t_{Irev} = 0.01$ s 	0.8°	3.0 s
50 rpm (0.105 m/s)	$t = 0.05$ s 	$T_{Irev} = 0.05$ s 	5°	1.2 s
100 rpm (0.21 m/s)	$t = 0.10$ s 	$T_{Irev} = 0.01$ s 	20°	0.6 s
155 rpm (0.324 m/s)	$t = 0.05$ s 	$t_{Irev} = 0.05$ s 	48°	0.38 s

3.3 Effect of Rotational Velocity on the Plasma Flow Characteristics

Table 1 summarizes the plasma flow characteristics under various rotational velocities, including the side and plane temperature rise images, the angle between the wear track and the plasma flow direction, α , and the time of one revolution of the disk rotation, t_{Irev} . It can be clearly seen in the side images that the plasma flow is lamellar under $V=0.021$ m/s ($\omega=10$ rpm), which turns to the turbulent one under $V=0.042$ m/s ($\omega=20$ rpm) and over. The turbulent plasma flow becomes more violent and the flow is stretched, elongated, and torn off to the rear ward with the increase of the rotational velocity, i.e., with the pin sliding velocity. You can see that the plasma is also generated in front of the sliding contact as clearly seen at $\omega=155$ rpm ($V=0.324$ m/s) and also scarcely in 20 rpm ($V=0.042$ m/s) in the side images. Most of the tribocharges produced at the sliding contact are consumed for generating the great rear plasma. However, part of the tribocharge remains on the wear track surface without full consumption at the rear plasma generation. The remained charges come to the front gap of the sliding contact by rotation of the disk. By this remained tribocharge, the front triboplasma is generated as described above.

On the other hand, the plane images show that the plasma flows along the wear track in the lamellar flow under 10 rpm ($V=0.021$ m/s), the direction of which shifts to clockwise to the disk rotation direction under the higher rotational velocities of 20 rpm ($V=0.042$ m/s), 50 rpm ($V=0.105$ m/s), 100 rpm ($V=0.21$ m/s), and 155 rpm ($V=0.324$ m/s) in the

turbulent flow regime. The angle between the plasma flow direction and the wear track, α , increases with the rotational velocity to reach the value of $\alpha=48^\circ$ at $\omega=155$ rpm. The increase of the value of α must be caused by the increase of the centrifugal forces expressed by $F=m\omega^2r$, where m is the mass of plasma, r is the wear track radius, and ω is the rotational velocity. The values of α at 50, 100, and 150 rpm were the experimentally measured one, but those at 10 and 20 rpm were the one calculated from the centrifugal force because their experimental values were too small to be measured.

The tribosystem of the head-disk-interface (HDI) in the hard-disk drives (HDDs), where the head made of $\text{Al}_2\text{O}_3/\text{TiC}$ composite coated by DLC film slides against the rotating magnetic disk coated with DLC film, is almost in the same situation as that of the present experimental condition where the insulating diamond pin slides on the insulating rotating sapphire disk in dry sliding in the ambient air. The contact of the DLC film on the head sliding against the DLC film on the magnetic disk causes tribocharging to generate the triboplasma, the intensity of which is a function of the electric resistivity nature of the DLC film [11, 12]. In the case of the hydrogenated DLC film, the intensity of the triboplasma increases with the hydrogen content of the DLC film, since the electric resistivity increases with the hydrogen content [12]. Frequent contacts of the head and the rotating recording disk should take place at the so small gap of 1~2 nm under so high rotating velocities of the disk of about 7000 rpm to generate triboplasma in HDDs. The generated triboplasma itself should cause decomposition of the perfluoropolyether lubricating film coated on the rotating disk for preventing the wear of the DLC film under the

contact pressure of 1~2 GPa at the asperity contact [13] in HDDs [14], whereas the triboplasma flow transition from the lamellar to the turbulent flow should take place at the start and stop of the operation of HDDs, leading to the problems in the stability of the HDI. The triboplasma flow behaviors can be investigated in various situations including the HDDs using the warmed specimens by a microscopic sensitive infrared camera.

4 Conclusions

The flow characteristics of the triboplasma were investigated by measuring the temperature rise distribution of the triboplasma generated in the gap of the sliding contact in the tribosystem where the warmed diamond pin slides against the warmed sapphire disk in the ambient air in dry sliding using a microscopic infrared camera, and the following conclusions have been drawn.

- (1) The triboplasma flows out of the sliding contact in the two kinds of flow types: the lamellar flow and the turbulent flow. The lamellar flow takes place at and below the sliding velocity of $V=0.021$ m/s ($\omega=10$ rpm). This lamellar flow transits to the turbulent flow at and above the sliding velocities of $V=0.042$ m/s ($\omega=20$ rpm). The turbulent flow becomes more violent as the disk rotational velocity increases.
- (2) The plasma flows out along the wear track at and below the low rotational velocity of $\omega=10$ rpm ($V=0.021$ m/s). However, with the increase of the rotational velocity, the plasma flow direction shifts clockwise to the direction of the disk rotation at and above $\omega=20$ rpm ($V=0.042$ m/s) due to the centrifugal forces. The angle between the sliding direction and the plasma flow direction increases with the rotational velocity.
- (3) The size and the strength of the plasma flow changes with time. They increase with time to reach the maximum and then diminish. This time dependence nature is almost independent of the repeated sliding. This is because the plasma distribution is a function of the non-uniform tribocharge distribution, which is almost independent of the repeated sliding on the wear track surface.
- (4) The temperature rise distribution measurement using the warmed test specimen by the microscopic infrared

camera is a useful technique to investigate the triboplasma flow behaviors.

Acknowledgement The authors would like to express their thanks to the financial support by the Grant-in-aid for Scientific Research (A) 20246035, the Ministry of Education, Culture, Sports, Science and Technology.

References

1. Nakayama, K., Nevshupa, R.A.: Plasma generation in a gap around a sliding contact. *J. Phys. D* **35**, L53–56 (2002)
2. Nakayama, K., Yagasaki, F.: The temperature of triboplasma. *Tribol. Lett.* **66**, 10 (2018)
3. Finkelnburg, W., Segal, S.M.: High temperature plasma properties from high current arc stream measurements. *Phys. Rev.* **80**, 258 (1950)
4. Bikerton, R.J.: Introduction to high temperature plasma physics. *Philos. Trans. R. Soc. Lond.* **300**, 475–488 (1981)
5. Report of the department of energy office of fusion energy sciences, *Low temperature plasma science: not only the fourth state of matter but all of them* (Workshop on Low Temperature Plasmas) (2008)
6. Becker, K.H., Kogelshatz, U., Schoenbach, K.H., Barker, R.H.: *Non-equilibrium Air Plasmas at Atmospheric Pressure*. Institute of Physics, CRC Press, Boca Raton (2004)
7. Yang, Y., Cho, Y.I., Friedman, A.: *Plasma Discharge in Liquid: Water Treatment and Applications*. CRC Press, Boca Raton (2012)
8. Nakayama, K., Fujimoto, T.: The energy of electrons emitted from wearing solid surfaces. *Tribol. Lett.* **17**, 75 (2004)
9. Cameron, A.: *The Principles of Lubrication*. Longmans, London (1966)
10. Moore, D.S.: *Principles and Application of Tribology*. Pergamum International Library, Oxford (1975)
11. Nakayama, K.: Triboemission of charged particles and resistivity of solids. *Tribol. Lett.* **6**, 37 (1999)
12. Nakayama, K.: Triboemission of electrons, ions, and photons from diamondlike carbon films and generation of triboplasma. *Surf. Coat. Technol.* **188–189**, 599 (2004)
13. Ikeda, K., Ono, K.: Design consideration of contact/near-contact slider based on a rough surface contact model. *Trans. Jpn. Soc. Mech. Eng. C* **68**, 1518 (2002)
14. Nakayama, K., Mirza, S.M.: Verification of the decomposition of perfluoropolyether fluid due to triboplasma. *Tribol. Trans.* **49**, 17 (2006)

Publisher's Note Springer Nature remains neutral with regard to jurisdictional claims in published maps and institutional affiliations.